Imaging local diffusion in microstructures using NV-based pulsed field gradient NMR

Short title: NV-based diffusion imaging in microstructures

F. Bruckmaier[1], R. D. Allert[1], N. R. Neuling[1], P. Amrein[2], S. Littin[2], K. D. Briegel[1], P. Schätzle[3], P. Knittel[4], M. Zaitsev[2], D. B. Bucher[1,5]*

[1]Chemistry Department, TUM School of Natural Sciences, Technical University of Munich, Germany
[2]Department of Radiology, University Medical Center Freiburg, Germany
[3]University of Freiburg, Department of Sustainable Systems Engineering (INATECH), Emmy-Noether-Str. 2, 79110
[4]Fraunhofer Institute for Applied Solid State Physics, Tullastr. 72, 79108 Freiburg, Germany
[5]Munich Center for Quantum Science and Technology (MCQST), Schellingstr. 4, 80799 München, Germany
*Corresponding author: Prof. Dr. Dominik Bucher; E-mail: Dominik.Bucher@tum.de

Understanding diffusion in microstructures plays a crucial role in many scientific fields, including neuroscience, cancer- or energy research. While magnetic resonance methods are the gold standard for quantitative diffusion measurements, they lack sensitivity in resolving and measuring diffusion within individual microstructures. Here, we introduce nitrogen-vacancy (NV) center based nuclear magnetic resonance (NMR) spectroscopy as a novel tool to probe diffusion in individual structures on microscopic length scales. We have developed a novel experimental scheme combining pulsed gradient spin echo (PGSE) with optically detected NV-NMR, which allows for the quantification of molecular diffusion and flow within nano-to-picoliter sample volumes. We demonstrate correlated optical imaging with spatially resolved PGSE NV-

NMR experiments to probe anisotropic water diffusion within a model microstructure. Our method will extend the current capabilities of investigating diffusion processes to the microscopic length scale with the potential of probing single-cells, tissue microstructures, or ion mobility in thin film materials for battery applications.

Introduction

Molecular and ion diffusion plays a major role in many aspects of physics, chemistry, and biology, ranging from nutrient transport in organisms [*1, 2*], pattern formation [*3*], to the reactivity in chemical reactions [*4*] or the functioning of modern batteries [*5*]. Nuclear magnetic resonance (NMR) spectroscopy is one of the prevalent methods for probing diffusion [*6, 7*] which was first described in 1965 by Stejskal and Tanner [*8*]. Since then, the technique has developed rapidly and is nowadays used on a daily basis in the form of diffusion weighted magnetic resonance imaging in medicine [*9–14*]. However, magnetic resonance methods are limited by the low net nuclear magnetization of the sample, which results in a low sensitivity. Diffusion-weighted imaging further decreases the signal, limiting the achievable resolution to the sub-millimeter regime on applicable measurement time scales. For that reason, measuring diffusion with micrometer resolution within thin film materials, biological tissue or even for single cells is far out of reach.

An elegant solution to overcome the sensitivity problem of NMR is the nitrogen vacancy (NV) center in diamond which is an atom-sized quantum sensor for magnetic fields [*15, 16*]. Due to its spin state-dependent fluorescence, optically detected magnetic resonance (ODMR) experiments can be performed which translate the local magnetic field into an optical signal. NV-centers have been used to conduct NMR experiments on unprecedented length scales [*17–20*] and allow the detection of high spectral resolution NMR signals from picoliter sample volumes [*21–26*].

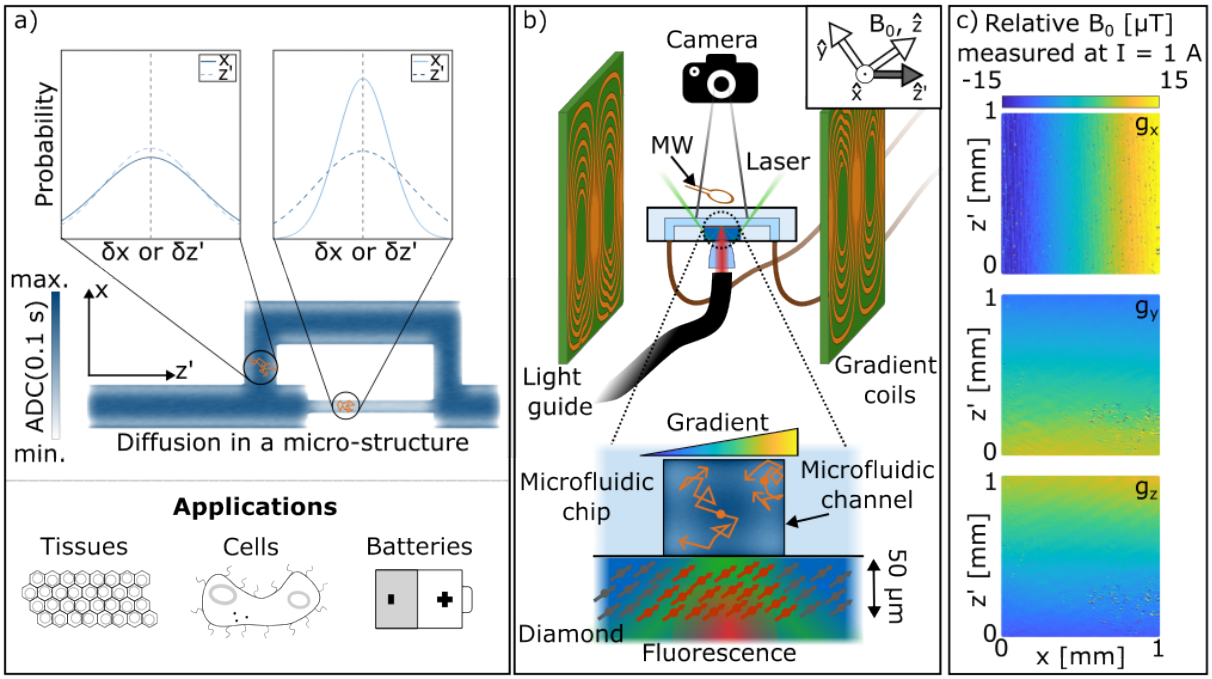

Figure 1: **Principles of NV-based diffusion imaging within microstructures. a)** Conceptual schematic of diffusion within a microstructure. The apparent diffusion coefficient (ADC) in the two marked locations differs strongly in the $\hat{x}$ and $\hat{z}$' directions, since the free diffusion length is on the same scale as the microstructure itself. The probability to find a diffusing particle at a distance $\delta\hat{x}$ ($\delta\hat{z}$', see b)) from its original position (grey line) after diffusing for 0.1 s is displayed in the two plots on the top. The microstructure itself is colored according to the simulated ADC. **b)** *Top*: Experimental setup. A diamond chip (dark blue) with a highly dense surface doped NV-layer is glued into the microfluidic chip (light blue) and placed in between three pairs of magnetic field gradient coils. Each pair produces a $\hat{B}_0$-gradient along one of the cardinal directions $\hat{x}$, $\hat{y}$ and $\hat{z}$. The whole experiment is imaged using an optical microscope from above. A laser (green) enters the diamond chip and excites the NV-centers in the surface layer, defining the measurement location. The red NV-fluorescence for signal readout is collected and directed to a photodiode using a liquid light guide. The NV electronic spin, used for the quantum sensing protocol is driven by a microwave (MW) antenna on top of the microfluidic chip. *Bottom*: The water sample is confined by a microfluidic channel, whose bottom wall is formed by the NV-sensor. Water molecules interacting with the channel walls are hindered in their diffusion and will have a lower ADC. External magnetic-field gradients encode the position of the water molecules and allow for the measurement of their ADCs. **c)** Measured B_0 gradients along the three cardinal directions (see b)) using an NV wide-field magnetic imaging setup.

This technology is an ideal candidate for the investigation of diffusion phenomena on the

microscopic level, due to its optical readout, high spatial resolution and capability of measuring coherent NMR signals. In contrast to macroscopic diffusion-based MR experiments, the NV-sensor enables the detection of the NMR signals on a length scale of the same order of magnitude as the average distance a water molecule will have diffused within the timescale of a typical NMR experiment. If the molecule encounters a barrier, the average displacement is reduced compared to the case of free diffusion. For that reason, microscale NV-NMR is the ideal tool for probing diffusion within microstructures, as shown in Fig. 1 a).

In this work, we realize microscopic imaging of molecular diffusion with NV-NMR. We first developed magnetic field gradient coils and designed pulse sequences that combine pulsed field gradients with the NV-NMR detection scheme. This allows us to perform pulsed gradient spin echo (PGSE) experiments to detect diffusion within picoliter sample volumes. In the first series of experiments, we measure the water flow within a microfluidic channel. The same approach is also used to detect water diffusion as a function of sample viscosity. Finally, we demonstrate the capabilities of our technique for detecting local water diffusion within a microstructure. Spatially resolved diffusion NV-NMR measurements within a microfluidic model structure show anisotropic diffusion according to the restrictions given by the local geometry and structure.

Results

The experimental setup developed for this publication is depicted in Fig. 1 b), which can be split into two parts - the diffusion encoding using magnetic field gradient pulses during a spin echo sequence and the detection of the corresponding NMR signal with an NV-ensemble. We use a highly doped NV-layer with a thickness of $\sim 50\,\mu$m that allows us to detect NMR signals on a similar length scale which also corresponds approximately to the typical diffusion displacement in our PGSE experiment [*21, 27*]. As a model system, we use microfluidic chips [*26*], where the NV-center layer forms the bottom wall of the microfluidic channel. The microflu-

idic chip is coupled to a syringe pump, allowing for precise control of the sample liquid. For the initialization and readout of the NV-center's quantum state for the NMR detection, a 532 nm laser is coupled into the trapezoid diamond via a total internal reflection geometry [*21*]. This reduces laser-induced sample damage and heating while increasing the laser-intensity at the NV-layer [*26*]. A custom compound parabolic concentrator is glued to the bottom side of the NV-diamond chip [*28*]. It efficiently collects the NV-fluorescence which is then directed to a photodiode via a liquid light guide [*29*]. The NV-diamond and microfluidic structure is imaged from the top, enabling us to correlate an optical image with the PGSE NV-NMR signal, defined by the location of the optical excitation. The free nuclear decay (FND) of the sample is induced by a radio frequency (RF) pulse and the corresponding NMR signal is detected via the NV ensemble, which is driven by microwave (MW) pulse sequence. The entire experiment is mounted within a large bore superconducting magnet, which provides a highly homogeneous and stable magnetic field B_0, crucial for the detection of the NMR signal.

For the PGSE experiment, a set of three pairs of gradient coils ($\hat{x}$, $\hat{y}$ and $\hat{z}$) were designed and fabricated using the openly available gradient coil design tool CoilGen [*30*]. These coils have to satisfy unique conditions of NV-NMR spectroscopy, such as the optical access from multiple sides and, most importantly, a gradient along the B_0-field orientation, tilted at an angle of $\sim 54.74^\circ$ to the diamond surface normal. This angle is defined by the orientation of the NV-centers within our diamond chip and, ultimately the crystal orientation of the diamond sensor [*27*]. The method for finding optimal current carrying surfaces for this setup is described in Amrein *et al.* [*31*]. Characterization was performed using ODMR of the NV-centers in a widefield approach [*32*], extracting the relative $\hat{B}_0$-amplitudes over the diamond by measuring the NV-center's Zeeman-splitting, resulting in gradient strengths of $g_x = 29.74 \pm 0.09 \, \frac{\mathrm{mT}}{\mathrm{A\,m}}$, $g_y = 25.92 \pm 0.09 \, \frac{\mathrm{mT}}{\mathrm{A\,m}}$ and $g_z = 23.27 \pm 0.06 \, \frac{\mathrm{mT}}{\mathrm{A\,m}}$, respectively. The experimental results are shown in Fig. 1 c).

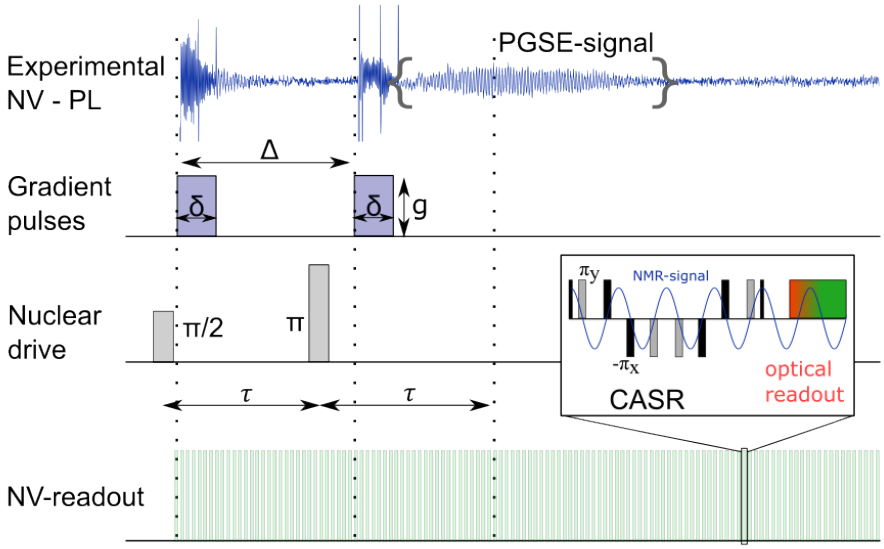

Figure 2: **Principle of the pulse gradient spin echo (PGSE) NV-NMR sequence**. A RF $\pi/2$-pulse at the Larmor frequency of the protons initializes the free nuclear precision. After a time τ, a π-pulse refocuses the sample nuclear spin magnetization leading to a spin echo (experimental data in blue). For the PGSE experiment, magnetic field gradient pulse with equal duration δ and strength g are applied before and after the nuclear spin π-pulse (blue), separated by a total time Δ. These magnetic field gradient pulses encode the position of the nuclear spins in their phase and any translation or diffusion during the time Δ will reduce the total spin echo signal. The ADC can be obtained by measuring the spin echo amplitude as a function of the applied magnetic field gradient strength δg. The spin echo NMR signal is read out by an NV-ensemble using the CASR pulse sequence, which consists of a train of single dynamic decoupling sequences. *Insert:* A single dynamic decoupling subsequence, which consists of a train of π-pulses on the NV electronic spin, synchronized to the Larmor frequency of the nuclear spins. Typical parameter values used in this work are $\delta = 10$ ms, $\Delta = 80$ ms and $\tau = 75$ ms, whereas the gradient strength is swept from $g = 0$ mT/m to $g = 25$ mT/m.

For the NMR signal detection, we use the coherently averaged synchronized readout (CASR) method [*21*] (see Fig. 2). It consists of a train of dynamic decoupling sequences which is synchronized to the sample FND. The detected signal of the optical NV readouts using CASR is an aliased version of the NMR signal. A more in-depth explanation of the sensing scheme is described in Glenn *et al.* [*21*]. All experiments described in this work were conducted on

protons in water, which were detected at a resonance frequency of $\sim$7.45 MHz (B_0 of $\sim$0.175 T). To increase the NMR signal and reduce the averaging time, Overhauser dynamic nuclear hyperpolarization (DNP) was used in all experiments [*24, 33*].

The diffusion-NMR method used in this paper is called pulsed gradient spin echo (PGSE) [*8*]. This sequence is a modification of the classic spin-echo experiment, where before and after the refocusing π-pulse two identical spatially varying B_0-gradient pulses are applied. The magnetic field gradient causes a spatially dependent Larmor frequency shifts which encodes the position of the nuclear sample spins. The first gradient pulse leads to a relative phase-accumulation of each individual sample spin depending on its position, and the second gradient pulse leads to an inverse phase accumulation or refocusing up to the amount each spin has diffused along the gradient in the time between the two pulses. In the limit where the pulsed gradient amplitude is much higher than the constant background gradient of the magnetic field, the diffusion coefficient D can be extracted by sweeping the strength of the applied gradient according to:

$$D = -\ln(A/A_0)\left[(\delta\, g\, \gamma)^2\left(\Delta - \frac{\delta}{3}\right)\right]^{-1}, \tag{1}$$

here A and A_0 are the spin echo amplitudes with and without gradient pulses, respectively, δ is the duration, Δ is the spacing, g is the strength of the applied gradient pulses and γ is the gyromagnetic ratio of the sample spins [*8*]. Figure 2 shows the corresponding pulse sequence and an experimental data set of PGSE NV-NMR experiment. For restricted diffusion, as is the case in our microfluidic channel, a slightly modified model including tensor properties of diffusion needs to be used to determine the apparent diffusion coefficient (ADC), which can be found in the SM, section 2. Individual tensor elements can be measured, by changing the direction of the first and/or second gradient pulse. The gradient directions used in this work are 1) parallel to B_0 ($\hat{z}$), 2) orthogonal to B_0 and parallel to the diamond surface ($\hat{x}$) and 3) the remaining direction at a $\approx$35.26° angle to the diamond surface normal ($\hat{y}$), as depicted in Fig. 1 b).

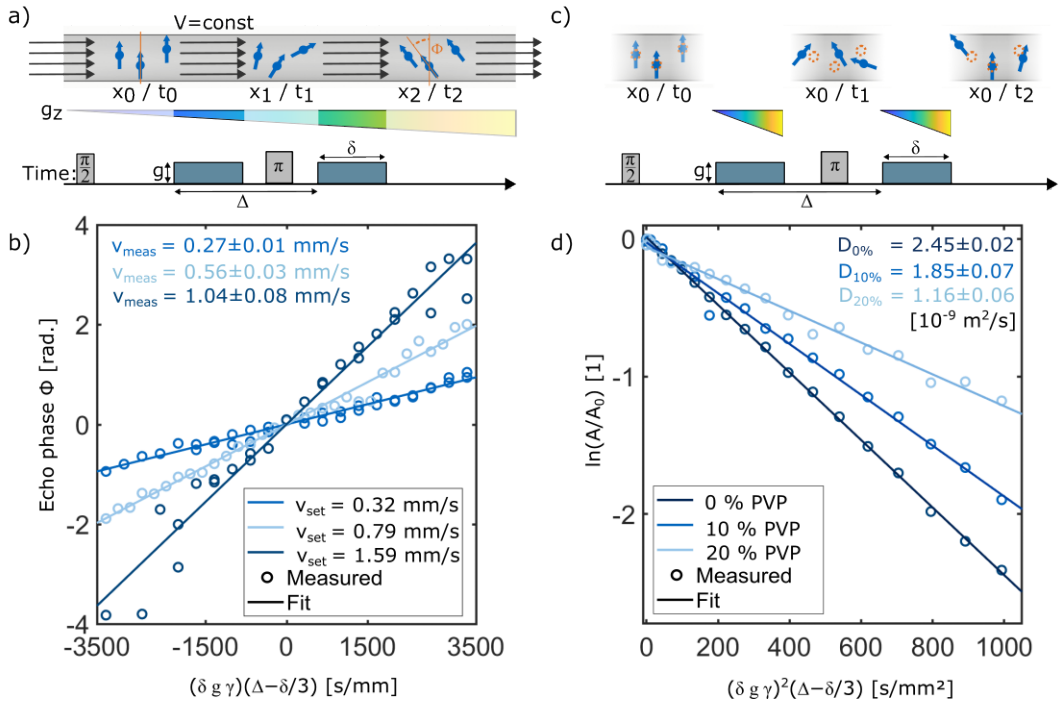

Figure 3: **Measuring water flow and diffusion using PGSE NV-NMR a)** Schematic of sample spins moving in a microfluidic channel during a velocimetry measurement. During the PGSE experiment a constant and laminar flow is applied which will lead to an equal translation of all sample molecules from their initial, $t = t_0$, location x_0 to their final position x_2 at $t = t_2$. This leads to an equal shift in each sample-spin's phase which depends on the translated distance between the two gradient pulses and the strength and duration of the individual pulses. The PGSE-sequence is sketched in the bottom, the absolute gradient-strength of each pulse is colour coded. **b)** Experimental data (phase ϕ as a function of gradient amplitude g) (circles) and fits (lines) for three different flow rates. Increasing the gradient amplitude leads to a larger phase accumulation due to the flow in the channel. **c)** Molecular diffusion leads to a random displacement of the sample spins which effectively attenuates the amplitude of the PGSE. The PGSE-sequence is sketched in the bottom of the figure. **d)** Three PGSE measurements (sweeping the gradient strength) of different concentration of polyvinylpyrrolidone (PVP) K90 in water. The normalized spin echo amplitudes are displayed as circles and linear fits as dashed lines.

In the first set of experiments we used our PGSE NV-NMR setup to measure the flow velocity of water within our microfluidic channel. Assuming a homogeneous flow profile, each molecule of water will have moved the same distance along the gradient during the free-

diffusion time Δ. This causes a common relative phase shift ϕ (Fig. 3 a)) of the nuclear spins. Since the NV-NMR detection method used for our experiments is phase sensitive [*21*], the water flow within the channel can be calculated from the applied magnetic field gradient.
Including laminar flow into equation 1, the combined effects of diffusion and translation on the sample magnetization can be described as [*9, 12*]:

$$A/A_0 = \exp\left((i\ v - D\ \gamma \mathrm{g}\delta)(\gamma \mathrm{g}\delta)(\Delta - \delta/3)\right)\ , \tag{2}$$

where v is the flow-velocity within the channel and i is the imaginary unit. The signal phase $\phi = v\gamma g\delta(\Delta - \delta/3)$ can be extracted from the experimental data via the imaginary and real part of the spin echo's Fourier transformation. Plotting the phase ϕ against the magnetic field gradient strength allows us to determine the velocity from a linear fit [*12*].

ADC$_z$ $[10^{-9}\, m^2/s]$ at $\sim$25° C	0 % PVP	10 % PVP	20 % PVP
Literature	2.31	1.81	1.37
Simulation	2.14	1.69	1.13
Experimental result	2.45±0.02	1.85±0.07	1.16±0.06

Table 1: **Results of the PVP diffusion measurements.** Literature [*34–36*], simulated and measured values of the ADC for three different concentrations of PVP in water (w/w) with their respective uncertainties.

The experiments were conducted in a straight microfluidic channel with dimensions of 80 μm (orthogonal to the diamond surface) x 100 μm (along the $\hat{x}$-direction) x 2 mm (along the $\hat{z}'$-direction). The experimentally measured flow rates by PGSE NV-NMR were 0.27 ± 0.01 mm/s, 0.56 ± 0.03 mm/s and 1.04 ± 0.08 mm/s, which are slightly but consistently lower than the parameters set at the syringe pump used in this experiment 3 b). This can be explained by an additional layer of glue in between the diamond and the microfluidic chip: The flow-rate in the microfluidic channel is calculated from the flow-rate set at our pump, given in units of $\frac{volume}{time}$. This is divided by the intended cross-section of the microfluidic channel, resulting in the flow-

rates v_{set} as seen above. Any difference between the cross-section of the microfluidic channel in the experiment and as designed would lead to a proportional offset between measured and set flow-rates.

In the second set of experiments, we measured the diffusion coefficient of water in the microfluidic channel. In contrast to the laminar flow in the previous experiment, diffusion leads to random motion and a reduction of the spin echo as a function of gradient strength (Figure 3 c)). We used water with different concentrations (0%, 10% and 20% w/w) of polyvinylpyrrolidone K90 (PVP) at T $\approx$25° C, an organic polymer, to change the sample's viscosity and, thus, the diffusion coefficient, which had been investigated in detail before [*34–37*]. Since we measure the water diffusion within a microfluidic channel, the free diffusion will be attenuated by its boundaries. For that reason, we chose to sweep the amplitude of the g_z gradient to measure the ADC, since the diffusion along this direction is the least restricted therefore the closest to the values reported in the literature. Nevertheless, the boundaries of the microfluidic channel will reduce the ADC's diagonal elements, compared to the free diffusion case. Therefore, we simulated the expected ADC based on the literature values as described in the SM, section 2. The resulting data can be found in table 1 and seen in Fig. 3 d). The expected and simulated values are in good agreement with the values obtained from experimental PGSE NV-NMR. The remaining discrepancy between measured and simulated parameters can be explained by possible sample heating, as discussed in the SM, section 4, which affects the diffusion in solutions with higher concentrations of PVP to a lesser degree [*37*].

Having established the ability to perform PGSE experiments in combination with NV-NMR, allows us to probe water diffusion spatially resolved within microstructures. For that purpose, we designed and fabricated a microfluidic structure with different channel sizes and orientations. Due to the optical readout of the PGSE NV-NMR signal, any location within this structure can be probed by moving the NV-excitation laser (Fig. 4 a) and b)).

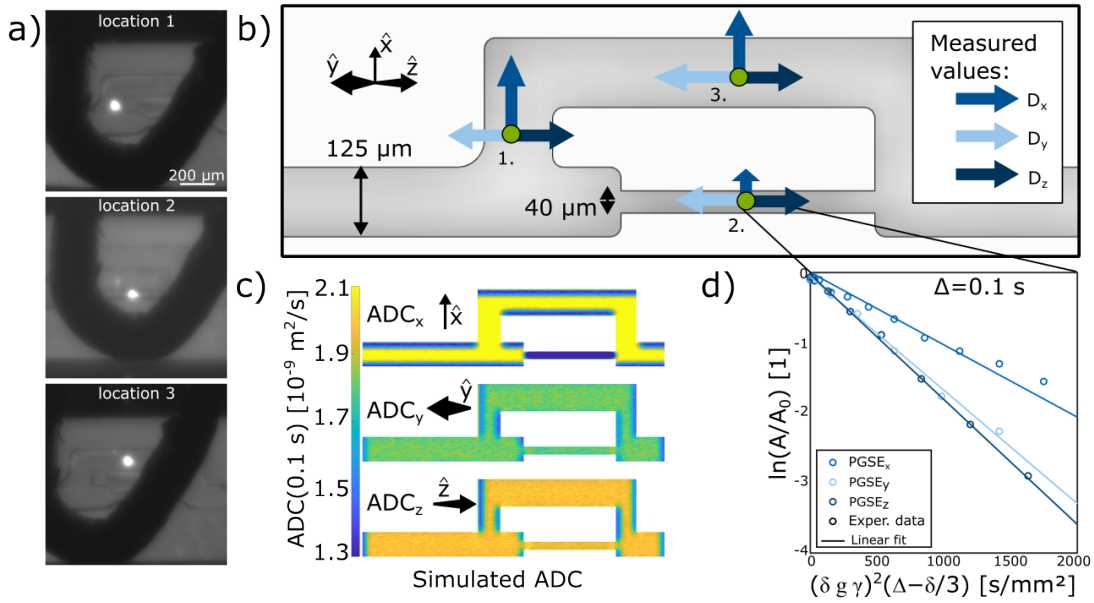

Figure 4: **Spatially resolved PGSE NV-NMR experiments within microfluidic structures a)** Photographs of our microfluidic chip and the three probed locations. **b)** Corresponding drawing of the microfluidic model structure. The local ADCs can be detected spatially resolved by moving the laser location (locations 1, 2 and 3). The experimental values correspond to the arrow length and are summarized in table 1). Please note that the y (light blue) and z (dark blue) directions are not in the image plane. **c)** Simulations of the ADC in the microfluidic channel along the $\hat{x}$, $\hat{y}$ and $\hat{z}$ directions. The effects of the diffusional anisotropicity due to the microstructure is visible, especially when comparing the ADC in the three directions in location 2: here the diffusion along $\hat{x}$ is strongly attenuated by the molecule's interacting with the channel walls, whereas the diffusion along $\hat{y}$ and $\hat{z}$ is comparable to the wider parts of the microstructure. **d)** Exemplary data set (location 2) where the ADC along the $\hat{x}$-direction is lower than along the $\hat{y}$ and $\hat{z}$-directions due to the channel constraints.

For an estimation of the expected ADC within our microfluidic structure, the ADC for each point was simulated using particles undergoing a random walk. Due to the small length scales, the ADC along the different cardinal directions can vary drastically (Fig. 4 b). Then, we performed PGSE NV-NMR experiments at three different locations and along three different directions within this structure (Fig. 4 b). The ADC changes depending on the channel dimensions at the location of our laser within the structure, in accordance with our simulation (Fig. 4 c)). The difference is most pronounced when measurement locations 1 and 3 are compared

with location 2 along the $\hat{x}$ direction. In the narrow channel the water diffusion is restricted by the small length scale (L_2 $\sim$40 μm) whereas the other two locations have conditions close to the free diffusion. While the difference in the maximal free diffusion length L_i along $\hat{x}$ in location 1 (L_1 $\approx$300 μm) and 3 (L_2 $\approx$125 μm) differs by a significant amount, we still only detect a small difference in the ADC. The reason for these similar experimental values is, that the mean distance traveled by molecules during the free diffusion time Δ of our experiments is ≈ 25 μm$\ll L_1,\ L_2$. Therefore most molecules within the sample volume of either location will not have interacted with the boundaries of our microfluidic channel and the ADC is close to the free diffusion constant. Due to current limitations of the experimental setup, it was not possible for us to sweep the free diffusion time Δ in the PGSE NV-NMR experiment.

ADC $[10^{-9}\, m^2/s]$ at $\sim$25° C		Location 1	Location 2	Location 3
ADC_x	simulated	2.12 ± 0.10	1.25 ± 0.1	1.78 ± 0.10
	measured	2.56 ± 0.33	1.16 ± 0.18	2.11 ± 0.14
ADC_y	simulated	1.68 ± 0.10	1.78 ± 0.1	1.84 ± 0.10
	measured	1.97 ± 0.22	2.22 ± 0.21	2.67 ± 0.34
ADC_z	simulated	1.73 ± 0.10	1.94 ± 0.10	2.68 ± 0.08
	measured	1.96 ± 0.18	1.99 ± 0.06	2.00 ± 0.30

Table 2: **Results of the spatially resolved PGSE NV-NMR experiments within the microfluidic structure.** Measured and simulated diagonal elements of the ADC-tensor for each of the locations investigated. A detailed table with the fitted results of all measurements can be found in the SM, section 5.

Discussion

In this work, we have demonstrated spatially resolved PGSE-experiments within microstructures using NV-centers in diamond. We would like to note that the spatial resolution has not yet reached any physical limitations. Higher spatial resolution can be achieved by decreasing the thickness of the diamond's NV-center doped layer and reducing the diameter of the exci-

tation laser beam. In our current experimental setup, both the NV-center doped layer and the diameter of the laser location are on the order of ~ 50 μm, limiting our spatial resolution to the same order of magnitude [*27*]. Reaching the optical diffraction limit is feasible, although with the drawback of highly reduced sensitivity which would lead to long averaging times, as discussed in the SM, section 3. Nevertheless, this technique could enable quantifying the diffusion properties of basic micro-structural building blocks on the single cell level, which would help to validate current models in medical MRI [*38, 39*]. However, for biological applications Overhauser DNP used in our study is not recommended due to the need for spin labels within the sample. Alternatives are increasing the magnetic field B_0 strength (e.g. to 1 T) or other, bio-compatible hyperpolarization methods [*40*] (for instance, dissolution DNP or parahydrogen induced hyperpolarization, PHIP [*22*]). The latter methods allow for high signal enhancements that would allow for probing the diffusion of metabolites in single cells.

Another unique feature of our method is the possibility of applying ultrastrong magnetic field gradients [*41*]. Due to the small length scale of NV-NMR, gradient coils can be miniaturized, which can achieve up to 10.000 T/m [*42, 43*]. This would enable unique insights, e.g. in detecting slowly diffusing spins [*44, 45*] (such as Li-ions in solid state materials), in detecting diffusion on smallest length scales, or elucidating the origin of "dot-compartments", small diffusion restricted spaces in tissues, which are currently discussed in literature [*46*].

In summary, we have developed a novel NV-based NMR method, which enables us to image diffusion on the microscale. The technique allows the detection of water flow and diffusion within nano-to-picoliter sample volumes. Finally, we demonstrated the capability to measure the ADC spatially resolved within a model microstructure in three directions, which showed restriction in diffusion due to the local geometry. Our technique and experiments mark a major milestone towards probing tissue microstructures on the cellular level for understanding physi-

ology and pathology or novel ion-conducting materials in energy research.

Materials and Methods

Experimental setup. A schematic of the experimental setup and its optics is shown in the SM, section 1, Fig. S1 and S2. An electronic-grade, single crystal, 100-oriented diamond (2x2x0.5 mm, Element Six, Oxford, UK) which has been overgrown with a $\sim$ 19 ppm nitrogen-doped ^{12}C and ^{15}N isotopically enriched diamond layer with a thickness of $\sim 50\ \mu m$ by the Fraunhofer Institute for Applied Solid State Physics (Freiburg, Germany) as described in Schätzle *et al.* [*47*] and cut into a trapezoidal shape, which was then electron irradiated and annealed to increase the nitrogen to NV conversion rate. This particular thickness of the nitrogen doped layer was chosen, since simulations of the experimental geometry indicated this to optimize the signal to noise ratio (SNR) for our microfluidic channels [*26*]. Ramsey and Hahn echo spectroscopy is used to measure an NV ensemble T_2^* dephasing time of $\sim$0.65 μs and T_2 decoherence time of $\sim$ 9 μs, respectively. The diamond was glued into a microfluidic chip designed in house and fabricated by LightFab GmbH (Aachen, Germany) using Norland Optical Adhesive 68 UV-curing glue [*26*]. The assembled microfluidic chip with diamond was positioned in a custom build superconducting magnet (3T-215-RT, Superconducting Systems INC., Billerica, USA) and one of the four possible NV orientations with the diamond lattice was aligned with the external magnetic field ($B_0 \approx 0.175$ T). Flow pumps (AL-1000, World Precision Instruments, Sarasota, USA) were used to control the flow velocity within the microfluidic channel. The diamond's fluorescent light was collected using a compound parabolic concentrator (CPC) glued to the bottom of the microfluidic chip (designed in house and fabricated by Süd-Optik Schirmer GmbH, Kaufbeuren, Germany). The CPC output was attached to a custom made liquid light guide (Lumatec GmbH, Munich, Germany) which directs the fluorescence outside of the magnet through a long pass filter (BLP01-647R-25, Edge Basic 647 Long Wave Pass, Semrock,

Rochester, USA) onto a balanced photodiode (PDB210A, Thorlabs, Bergkirchen, Germany). A reference laser beam was used for efficient laser noise cancellation. The photodiode's voltage was read out using a data acquisition unit (NI USB-6821, National Instruments, Austin, USA). The NV-center spins were initialized using a $532\ nm$ laser (Laser Quantum Opus 53, Novanta Photonics, Wackersdorf, Germany) with a power of about ~ 380 mW. Initially the laser passes an opto-acoustic modulator (3260-220, Gooch and Housego, Ilminster, UK) to generate pulses of a typical length of $5\ \mu s$. A multi-order half-wave plate (WPMH05M-532, Thorlabs, Bergkirchen, Germany) was used to adjust the polarization of the laser light for efficient NV-excitation. Finally, the laser beam was expanded (BE02-05-A, Thorlabs, Bergkirchen, Germany) and focused onto the diamond using a $f = 250$ mm lens (LA1433-B-ML, Thorlabs, Bergkirchen, Germany), resulting in a beam diameter of $1/e^2 \approx 45\,\mu$m FWHM. The position of the laser location within the microstructure was imaged from the top on a camera (a2A3840-45umBAS, Basler, Ahrensburg, Germany).

The whole experimental sequence was controlled by an arbitrary waveform generator (AWG70000B, Tektronix, Beaverton, USA). It synchronizes all other devices (signal sources, switches, data acquisition unit and opto-acoustic modulator) via synchronised transistor transistor logic (TTL) signals (SM, section 1 Fig. S2). The pulse sequence, driving the NV-center's spins, is programmed and uploaded with a 500 MHz carrier frequency and up-converted using an IQ-mixer (mmiq0218LXPC, Marki Microwave, Morgan Hill, USA) and a MW signal source (SMB100A, Rhode und Schwarz, Munich, Germany). The resulting MW pulses were then amplified using a broadband $50\ W$ amplifier (AMP1016, Exodus, Las Vegas, USA) and delivered using a home-built microwave antenna [*48*]. A RF source (LXI DG1022, Rigol, Suzhou, China) was amplified (LZY-22+, Mini-Circuits, Brooklyn, USA) and connected to two coils in a Helmholtz-geometry with radius $R = 1.5$ cm for driving the sample nuclear spins with Rabi frequencies up to 6.3 kHz. An additional coil for calibration purposes was connected to another RF source (LXI

DG1022, Rigol, Suzhou, China), to determine the sensitivity of our experiment as described in Glenn *et al.* [*21*]. A third RF source (LXI DG1022, Rigol, Suzhou, China) was used to generate the gradient pulses which were fed into a bipolar power supply (BOP 5-20DL, Kepco, Naju, South Korea) capable of $\pm$ 20 V and $\pm$ 5 A, which in turn was connected to the gradient coils (Beta-Layout, Aarbergen, Germany). The microfluidic chip, MW, RF and gradient coils were all mounted on a custom designed, 3D-printed sample holder (grey v4 resin, Form 3, Formlabs, Somerville, USA). A photo of the setup and the assembly is depicted in the SM, section 1, Figure S3. To achieve a stronger NMR signal, Overhauser DNP was used [*24*]. In all experiments a 10 mM concentration of 4-Hydroxy-2,2,6,6-tetramethylpiperidin-1-oxyl (TEMPOL, 581500, Sigma-Aldrich, St. Louis, USA) was added to the respective sample. TEMPOL is a stable radical, which under continuous, strong and resonant MW-radiation ($0.3\,\mathrm{s}$) can hyperpolarize the nuclear sample spins, leading to a ~ 200-fold increase in the NMR-signal strength [*24*].

Gradient coil design. A Matlab-based software package [*30*] based on the stream function method [*49*] was used for the design of the gradient system. A biplanar configuration was chosen for the geometry of the gradient coils since it allows for better access for the fluorescence optical readout path compared to other geometries. Searching for a suitable biplanar configuration, several geometrical parameters were investigated such as plate size, plate distance and plate orientation and after evaluation, a solution with a plate size of 50 mm, a plate distance of 30 mm and an atypical azimuth plate tilt of 35.26° against the B_0 magnetic field was selected for printed circuit board (PCB) fabrication. Although the value of 35.26° for the azimuthal inclination is not optimal for the gradient's strength (the optimum is found at 55°), the gradient plates mounted vertically present a reasonable compromise between the achievable performance and the compatibility with the NV-NMR experimental setup. Since the gradient coils are only added for diffusion weighting, thermal limitations are not expected if the duty cycles of the used MR sequence are sufficiently low. More information on the design can be found in the dedicated

publication by Amrein *et al.* [*31*].

Microscale NV-NMR using the CASR pulse sequence. For this work the universally robust dynamic decoupling sequence [*50*] containing 12 pulses is used, with typically 50 repetitions per π-pulse train, leading to ≈ 600 π-pulses per measurement step. A typical duration of our π-pulses is $\sim$ 30 ns. In the case of the CASR pulse sequence, a detuning δf to the peak frequency f_0 is detected typically in the range of $|\delta f| < 3000$ Hz [*21*]. The typical AC-sensitivity and volume normalized AC-sensitivity of our experiment were ~ 20 pT$/\sqrt{\text{Hz}}$ and ~ 5.6 nT $\sqrt{\mu\text{m}^3}/(\sqrt{Hz})$, respectively. An example of a CASR measurement using the universally robust dynamic decoupling-8 sequence is depicted in Fig. 2. More information on the CASR method can be found in Glenn *et al.* [*21*].

PGSE NV-NMR pulse sequence. Typical parameter values used in for the PGSE-sequence are $\delta = 10$ ms, $\Delta = 80$ ms and $\tau = 75$ ms, sweeping the gradient strength from $g = 0$ mT$/$m to $g = 25$ mT$/$m. Experiments were averaged 100 times each, usually waiting a total of 3 s in between averages, to allow relaxation of the sample nuclear spins to thermal equilibrium. The typical single-shot SNR of a hyperpolarized water NMR signal in our experiments was ~ 100. Typical coherence times of the water protons were $T_2* \approx 60$ ms, $T_2 \approx 80$ ms and $T_1 \approx 0.3$ s. T_2* is very likely limited by magnetic field inhomogeneities of our experimental setup, while T_2 and T_1 were limited through the addition of TEMPOL into the solution.

Wide-field gradient imaging using CW-ODMR. The magnetic field gradients, shown in Fig. 1 c), are measured by wide-field DC magnetic imaging using continuous-wave optically detected magnetic resonance (CW-ODMR) [*32*]. As sensor we use an electronic-grade diamond chip (1.9 mm x 1.9 mm x 0.5 mm) with a 14 μm thick, ^{12}C and ^{15}N isotopically enriched, nitrogen doped layer (nitrogen concentration $\sim$ 2.3 ppm), which was electron irradiated and annealed to increase the nitrogen to NV-center conversion rate. An external magnetic field B_0

of $\sim$ 4.4 mT is applied along the NV symmetry axis which lifts the degeneracy of the $\mathrm{m_s}$ = $\pm$ 1 states. For excitation green laser light (Saphire LPX, Coherent, Santa Clara, USA) is used to fully illuminate the diamond chip ($\sim$ 600 mW). Electron spin ground state $\mathrm{m_s}$ = 0 $\rightarrow$ $\pm$1 transitions are probed by sweeping an applied microwave field in 400 steps (200 steps for each transition) synchronized to the NV fluorescence readout. The NV spin driving field is produced by a signal source (SMB100A, Rhode und Schwarz, Munich, Germany), amplified (ZHL-16W-72+, Mini-Circuits, Brooklyn, USA) and delivered to the diamond sample by a MW antenna. The NV fluorescence was passed through a spectral filter (BLP01-647R-25, Edge Basic 647 Long Wave Pass, Semrock, Rochester, USA) and collected by a camera (a2A1920-160umBAS, Basler, Ahrensburg, Germany) with a magnification of 2.75. For the measurements, 4x4 pixels are binned on the camera, resulting in 480x304 data points. Each data point is recorded with an exposure time of 600 μs and 800 averages. Thus, we acquire an image stack with a depth of 400, where each pixel stack corresponds to a single CW-ODMR spectrum. Four different CW-ODMR spectra are recorded with and without (background) applying a current of one ampere to the $\hat{x}$, $\hat{y}$ and $\hat{z}$ gradient coils. The gradient fields along B_0 are obtained by fitting (double Lorentzian) the NV-resonance lines of the collected data after subtraction the B_0 background field. Magnetic field values are calculated for each pixel stack from the splitting of the $\mathrm{m_s}$ = $\pm$ 1 states ($2\gamma B_0$), resulting in a 2D magnetic field map. The fitted gradients in g_y and g_z direction were corrected using factors of $\frac{1}{\sin(35.26^\circ)}$ and $\frac{1}{\cos(35.26^\circ)}$ respectively, since the gradient direction is not parallel to the diamond surface. Any constant offset produced by the gradient coils can be neglected, since it will have a negligible effect on the echo amplitude of the sample magnetization.

Data analysis The PGSE experiments were typically averaged 100 times and the data from the end of the second magnetic field gradient pulse to the point in time, where the FND's spectral components where below the noise floor, usually after about 0.25-0.35 s, was used for analysis.

This window was zero filled to a total of three times the initial length and Fourier-transformed. The NMR signal peak was integrated and the resulting data was normalized to the data point with the highest signal amplitude, taking into account the possibility of constant background gradients. Finally the whole data set was fitted with the function G:

$$G(D, g, \delta g) = \ln(\exp\left(-D\left(\delta\gamma(g-\delta g)\right)^2(\Delta - \delta/3)\right) + \text{Offset}) \ . \tag{3}$$

Δ, δ and γ are known, the gradient amplitude g is swept. δg is a fit parameter which takes constant magnetic field inhomogeneities caused by magnetic susceptibility mismatches between sample, microfluidic and diamond chip into account.

Simulation of diffusion in a restricted volume The simulations done for this work are based on a random walk of individual sample particles, in a defined, micro-scale volume. In each iteration a Gaussian distributed, random distance in an equally distributed random direction is chosen and the particle is moved accordingly. If the path hits a boundary of the micro-scale bounding volume, the packet is reflected inwards the rest of the way. At each time step the root mean squared distance traveled can be calculated, which is directly related to the ADC. For more information see the SM, section 2.

Acknowledgements

This project was funded by the European Research Council (ERC) under the European Union's Horizon 2020 research and innovation program (grant agreement No 948049) and by the Deutsche Forschungsgemeinschaft (DFG, German Research Foundation) - 412351169 within the Emmy Noether program. D.B.B. acknowledges support from the DFG under Germany's Excellence Strategy—EXC 2089/1—390776260 and the EXC-2111 390814868.

P.A., S.L. and M.Z. acknowledge support of the German Federal Ministry of Education and Research (BMBF) grant number 13GW0356B.

Author contributions statement

D.B.B. conceived and supervised the study. F.B. designed and conducted the experiments and did all simulations and analytic derivations. R.D.A. and N.N. contributed to various parts of the experimental setup. R.D.A. designed the microfluidic chips with help from N.N. and F.B.. K.D.B. designed and N.N. conducted the wide-field ESR experiments. P.A., S.L. and M.Z. designed the gradient coils used in this experiment and helped with their characterization. P.K., P.S. and R.D.A. produced the diamonds used in the experiments. F.B. and D.B.B. analyzed and discussed the data and wrote the manuscript with inputs from all authors.

Additional information

All authors declare that they have no competing interests.
Additional information on this work can be found in the Supplementary Material.

Bibliography

References

1. Reynold Spector. Nutrient transport systems in brain: 40 years of progress. *Journal of neurochemistry*, 111(2):315–320, 2009.

2. V. Gulani, A.G. Webb, I.D. Duncan, and P.C. Lauterbur. Apparent diffusion tensor measurements in myelin-deficient rat spinal cords. *Magnetic Resonance in Medicine*, 45(2):191–195, 2001.

3. Amit N. Landge, Benjamin M. Jordan, Xavier Diego, and Patrick Müller. Pattern formation mechanisms of self-organizing reaction-diffusion systems. *Developmental Biology*, 460(1):2–11, April 2020.

4. Richard M Noyes. Models relating molecular reactivity and diffusion in liquids. *Journal of the American Chemical Society*, 78(21):5486–5490, 1956.

5. Ting-Feng Yi, Ting-Ting Wei, Ying Li, Yan-Bing He, and Zhen-Bo Wang. Efforts on enhancing the li-ion diffusion coefficient and electronic conductivity of titanate-based anode materials for advanced li-ion batteries. *Energy Storage Materials*, 26:165–197, April 2020.

6. Paul T. Callaghan. *Translational Dynamics and Magnetic Resonance*. Oxford University Press, September 2011.

7. Jeffrey J Neil. Measurement of water motion (apparent diffusion) in biological systems. *Concepts in Magnetic Resonance: An Educational Journal*, 9(6):385–401, 1997.

8. E. O. Stejskal and J. E. Tanner. Spin diffusion measurements: Spin echoes in the presence of a time-dependent field gradient. *The Journal of Chemical Physics*, 42(1):288–292, January 1965.

9. Davy Sinnaeve. The stejskal-tanner equation generalized for any gradient shape-an overview of most pulse sequences measuring free diffusion. *Concepts in Magnetic Resonance Part A*, 40A(2):39–65, March 2012.

10. Konstantin I. Momot and Philip W. Kuchel. PFG NMR diffusion experiments for complex systems. *Concepts in Magnetic Resonance Part A*, 28A(4):249–269, 2006.

11. Filip Szczepankiewicz, Carl-Fredrik Westin, and Markus Nilsson. Gradient waveform design for tensor-valued encoding in diffusion MRI. *Journal of Neuroscience Methods*, 348:109007, January 2021.

12. Nathan H. Williamson, Michal E. Komlosh, Dan Benjamini, and Peter J. Basser. Limits to flow detection in phase contrast MRI. *Journal of Magnetic Resonance Open*, 2-3:100004, June 2020.

13. Denis Le Bihan. Looking into the functional architecture of the brain with diffusion MRI. *Nature Reviews Neuroscience*, 4(6):469–480, June 2003.

14. Henrik Lundell, Chloé Najac, Marjolein Bulk, Hermien E. Kan, Andrew G. Webb, and Itamar Ronen. Compartmental diffusion and microstructural properties of human brain gray and white matter studied with double diffusion encoding magnetic resonance spectroscopy of metabolites and water. *NeuroImage*, 234:117981, July 2021.

15. Gopalakrishnan Balasubramanian, I. Y. Chan, Roman Kolesov, Mohannad Al-Hmoud, Julia Tisler, Chang Shin, Changdong Kim, Aleksander Wojcik, Philip R. Hemmer, Anke Krueger, Tobias Hanke, Alfred Leitenstorfer, Rudolf Bratschitsch, Fedor Jelezko, and Jörg Wrachtrup. Nanoscale imaging magnetometry with diamond spins under ambient conditions. *Nature*, 455(7213):648–651, October 2008.

16. J. R. Maze, P. L. Stanwix, J. S. Hodges, S. Hong, J. M. Taylor, P. Cappellaro, L. Jiang, M. V. Gurudev Dutt, E. Togan, A. S. Zibrov, A. Yacoby, R. L. Walsworth, and M. D. Lukin. Nanoscale magnetic sensing with an individual electronic spin in diamond. *Nature*, 455(7213):644–647, October 2008.

17. C. Müller, X. Kong, J.-M. Cai, K. Melentijević, A. Stacey, M. Markham, D. Twitchen, J. Isoya, S. Pezzagna, J. Meijer, J. F. Du, M. B. Plenio, B. Naydenov, L. P. McGuinness, and F. Jelezko. Nuclear magnetic resonance spectroscopy with single spin sensitivity. *Nature Communications*, 5(1), August 2014.

18. A. O. Sushkov, I. Lovchinsky, N. Chisholm, R. L. Walsworth, H. Park, and M. D. Lukin. Magnetic resonance detection of individual proton spins using quantum reporters. *Phys. Rev. Lett.*, 113:197601, Nov 2014.

19. T. Staudacher, F. Shi, S. Pezzagna, J. Meijer, J. Du, C. A. Meriles, F. Reinhard, and J. Wrachtrup. Nuclear magnetic resonance spectroscopy on a (5-nanometer)3 sample volume. *Science*, 339(6119):561–563, 2013.

20. H. J. Mamin, M. Kim, M. H. Sherwood, C. T. Rettner, K. Ohno, D. D. Awschalom, and D. Rugar. Nanoscale nuclear magnetic resonance with a nitrogen-vacancy spin sensor. *Science*, 339(6119):557–560, January 2013.

21. David R. Glenn, Dominik B. Bucher, Junghyun Lee, Mikhail D. Lukin, Hongkun Park, and Ronald L. Walsworth. High-resolution magnetic resonance spectroscopy using a solid-state spin sensor. *Nature*, 555(7696):351–354, March 2018.

22. Nithya Arunkumar, Dominik B. Bucher, Matthew J. Turner, Patrick TomHon, David Glenn, Sören Lehmkuhl, Mikhail D. Lukin, Hongkun Park, Matthew S. Rosen, Thomas Theis, and Ronald L. Walsworth. Micron-scale nv-nmr spectroscopy with signal amplification by reversible exchange. *PRX Quantum*, 2:010305, Jan 2021.

23. Janis Smits, Joshua T. Damron, Pauli Kehayias, Andrew F. McDowell, Nazanin Mosavian, Ilja Fescenko, Nathaniel Ristoff, Abdelghani Laraoui, Andrey Jarmola, and Victor M. Acosta. Two-dimensional nuclear magnetic resonance spectroscopy with a microfluidic diamond quantum sensor. *Science Advances*, 5(7), 2019.

24. Dominik B. Bucher, David R. Glenn, Hongkun Park, Mikhail D. Lukin, and Ronald L. Walsworth. Hyperpolarization-enhanced NMR spectroscopy with femtomole sensitivity using quantum defects in diamond. *Physical Review X*, 10(2), June 2020.

25. Robin D. Allert, Karl D. Briegel, and Dominik B. Bucher. Advances in nano- and microscale NMR spectroscopy using diamond quantum sensors. *Chemical Communications*, 58(59):8165–8181, 2022.

26. R. D. Allert, F. Bruckmaier, N. R. Neuling, F. A. Freire-Moschovitis, K. S. Liu, C. Schrepel, P. Schätzle, P. Knittel, M. Hermans, and D. B. Bucher. Microfluidic quantum sensing platform for lab-on-a-chip applications. *Lab on a Chip*, 22(24):4831–4840, 2022.

27. Fleming Bruckmaier, Karl D. Briegel, and Dominik B. Bucher. Geometry dependence of micron-scale NMR signals on NV-diamond chips. *Journal of Magnetic Resonance Open*, 8-9:100023, December 2021.

28. Thomas Wolf, Philipp Neumann, Kazuo Nakamura, Hitoshi Sumiya, Takeshi Ohshima, Junichi Isoya, and Jörg Wrachtrup. Subpicotesla diamond magnetometry. *Phys. Rev. X*, 5:041001, Oct 2015.

29. Nithya Arunkumar, Kevin S. Olsson, Jner Tzern Oon, Connor Hart, Dominik B. Bucher, David Glenn, Mikhail D. Lukin, Hongkun Park, Donhee Ham, and Ronald L. Walsworth. Quantum logic enhanced sensing in solid-state spin ensembles, 2022.

30. Philipp Amrein, Feng Jia, Maxim Zaitsev, and Sebastian Littin. CoilGen: Open-source MR coil layout generator. *Magnetic Resonance in Medicine*, 88(3):1465–1479, May 2022.

31. Philipp Amrein, Fleming Bruckmaier, Feng Jia, Sebastian Littin, Dominik Bucher, and Maxim Zaitsev. Optimal bi-planar gradient coil configurations for diamond nitrogen-vacancy based diffusion-weighted nmr experiments. *Manuscript in preparation*, 2022.

32. Edlyn V. Levine, Matthew J. Turner, Pauli Kehayias, Connor A. Hart, Nicholas Langellier, Raisa Trubko, David R. Glenn, Roger R. Fu, and Ronald L. Walsworth. Principles and techniques of the quantum diamond microscope. *Nanophotonics*, 8(11):1945–1973, 2019.

33. F. A. L. Anet and A. J. R. Bourn. Nuclear magnetic resonance spectral assignments from nuclear overhauser effect. *Journal of the American Chemical Society*, 87(22):5250–5251, November 1965.

34. R. Mills. Self-diffusion in normal and heavy water in the range 1-45.deg. *The Journal of Physical Chemistry*, 77(5):685–688, March 1973.

35. Kenneth R. Harris and Lawrence A. Woolf. Pressure and temperature dependence of the self diffusion coefficient of water and oxygen-18 water. *Journal of the Chemical Society, Faraday Transactions 1: Physical Chemistry in Condensed Phases*, 76(0):377, 1980.

36. P.S. Tofts, D. Lloyd, C.A. Clark, G.J. Barker, G.J.M. Parker, P. McConville, C. Baldock, and J.M. Pope. Test liquids for quantitative MRI measurements of self-diffusion coefficient in vivo. *Magnetic Resonance in Medicine*, 43(3):368–374, March 2000.

37. Friedrich Wagner, Frederik B. Laun, Tristan A. Kuder, Anna Mlynarska, Florian Maier, Jonas Faust, Kerstin Demberg, Linus Lindemann, Boris Rivkin, Armin M. Nagel, Mark E. Ladd, Klaus Maier-Hein, Sebastian Bickelhaupt, and Michael Bach. Temperature and concentration calibration of aqueous polyvinylpyrrolidone (PVP) solutions for isotropic diffusion MRI phantoms. *PLOS ONE*, 12(6):e0179276, June 2017.

38. Els Fieremans and Hong-Hsi Lee. Physical and numerical phantoms for the validation of brain microstructural MRI: A cookbook. *NeuroImage*, 182:39–61, November 2018.

39. Dmitry S. Novikov, Els Fieremans, Sune N. Jespersen, and Valerij G. Kiselev. Quantifying brain microstructure with diffusion MRI: Theory and parameter estimation. *NMR in Biomedicine*, 32(4), October 2018.

40. James Eills, William Hale, and Marcel Utz. Synergies between hyperpolarized NMR and microfluidics: A review. *Progress in Nuclear Magnetic Resonance Spectroscopy*, 128:44–69, February 2022.

41. D.K. Jones, D.C. Alexander, R. Bowtell, M. Cercignani, F. Dell'Acqua, D.J. McHugh, K.L. Miller, M. Palombo, G.J.M. Parker, U.S. Rudrapatna, and C.M.W. Tax. Microstructural imaging of the human brain with a 'super-scanner': 10 key advantages of ultra-strong gradients for diffusion MRI. *NeuroImage*, 182:8–38, November 2018.

42. H. Zhang, K. Arai, C. Belthangady, J.-C. Jaskula, and R. L. Walsworth. Selective addressing of solid-state spins at the nanoscale via magnetic resonance frequency encoding. *npj Quantum Information*, 3(1), August 2017.

43. K. Arai, C. Belthangady, H. Zhang, N. Bar-Gill, S. J. DeVience, P. Cappellaro, A. Yacoby, and R. L. Walsworth. Fourier magnetic imaging with nanoscale resolution and compressed sensing speed-up using electronic spins in diamond. *Nature Nanotechnology*, 10(10):859–864, August 2015.

44. Hendrik H. Heenen, Christoph Scheurer, and Karsten Reuter. Implications of occupational disorder on ion mobility in $li_4ti_5o_{12}$ battery materials. *Nano Letters*, 17(6):3884–3888, May 2017.

45. Peter Benedek, Ola K. Forslund, Elisabetta Nocerino, Nuri Yazdani, Nami Matsubara, Yasmine Sassa, Fanni Jurànyi, Marisa Medarde, Mark Telling, Martin Månsson, and Vanessa Wood. Quantifying diffusion through interfaces of lithium-ion battery active materials. *ACS Applied Materials & Interfaces*, 12(14):16243–16249, 2020. PMID: 32163263.

46. Chantal M.W. Tax, Filip Szczepankiewicz, Markus Nilsson, and Derek K. Jones. The dot-compartment revealed? diffusion mri with ultra-strong gradients and spherical tensor encoding in the living human brain. *NeuroImage*, 210:116534, 2020.

47. Philip Schätzle, Philipp Reinke, David Herrling, Arne Götze, Lukas Lindner, Jan Jeske, Lutz Kirste, and Peter Knittel. A chemical vapor deposition diamond reactor for controlled thin-film growth with sharp layer interfaces. *physica status solidi (a)*, page 2200351, August 2022.

48. Dominik B. Bucher, Diana P. L. Aude Craik, Mikael P. Backlund, Matthew J. Turner, Oren Ben Dor, David R. Glenn, and Ronald L. Walsworth. Quantum diamond spectrometer for nanoscale NMR and ESR spectroscopy. *Nature Protocols*, 14(9):2707–2747, September 2019.

49. Rostislav A. Lemdiasov and Reinhold Ludwig. A stream function method for gradient coil design. *Concepts in Magnetic Resonance Part B: Magnetic Resonance Engineering*, 26B(1):67–80, 2005.

50. Genko T. Genov, Daniel Schraft, Nikolay V. Vitanov, and Thomas Halfmann. Arbitrarily accurate pulse sequences for robust dynamical decoupling. *Phys. Rev. Lett.*, 118:133202, Mar 2017.